A full three-dimensional characterization of defocusing digital particle image velocimetry

L Kajitani and D Dabiri

Department of Aeronautics and Astronautics, University of Washington, Box 352400,
Seattle, WA 98195, USA

E-mail: dabiri@aa.washington.edu

Abstract
The paradigm set forth by Pereira *et al* (2000 *Exp. Fluids* **29** S78–84)
was an important milestone in capturing the optical geometry of a three-
dimensional defocusing digital particle image velocimetry (DDPIV) design
within a set of systematic equations. However, the opportunity to improve
upon their pseudo-three-dimensional conceptual implementation of the
two-dimensional equations exists by revisiting the derivations of these
equations and revising some of their assumptions in order to define a
modified set of equations for a true full-three-dimensional derivation. This
paper introduces this newly revised set of equations that will explicitly and
more accurately represent the three-dimensional DDPIV measurement
system. A three-dimensional geometric uncertainty model has also been
established through uncertainty analysis. Finally, a discussion of the
differences and benefits of the new system of equations is presented.

(Some figures in this article are in colour only in the electronic version)

Nomenclature

γ	radial distance from the optical axis to the lenses
ζ	distance from an equilateral triangle's centre to any one of its vertices
a_{pf}	side-length of the front face of the volume of interest in the present derivation
a_{pb}	side-length of the rear face of the volume of interest in the present derivation
a_z	thickness of the volume of interest in the present derivation
b	image separation
c	side-length of the cubic domain of interest in the two-dimensional derivation
D	diameter of the lenses
d	distance between the lenses
f	focal length of the lenses
H	the height of the reference plane within the observable domain at the reference distance, L
h	photosensor size
k_X	resolution requirement constant for ΔX, generally defined to be 0.01 pixel
k_Z	resolution requirement constant for ΔZ, stipulated to be greater than zero
l	distance from the lenses to the CCD sensors along the optical axis
L	distance from the lens to the reference plane along the optical axis
M	optical magnification
X	X-coordinate of a particle in the global coordinate system
x_0	x-coordinate of an equilateral triangle's centre mapped by the triple CCDs' exposure of a particle in the local CCD coordinate system

x_B x-coordinate of the base vertex of the image in the local CCD coordinate system

x_{TL} x-coordinate of the top left vertex of the image in the local CCD coordinate system

x_{TR} x-coordinate of the top right vertex of the image in the local CCD coordinate system

Y Y-coordinate of a particle in the global coordinate system

y_0 y-coordinate of an equilateral triangle's centre mapped by the triple CCDs' exposure of a particle in the local CCD coordinate system

y_B y-coordinate of the base vertex of the image in the local coordinate system

y_{TL} y-coordinate of the top left vertex of the image in the local CCD coordinate system

y_{TR} y-coordinate of the top right vertex of the image in the local CCD coordinate system

Z Z-coordinate of a particle in the global coordinate system

Z_a location of the front face of the domain of interest relative to the lens plane

Z_{min} location of the intersection of the emerging rays from the lenses on the optical axis

1. Introduction

Particle image velocimetry (PIV) is a significant quantitative flow visualization technique used ubiquitously today due to its advantageous non-penetrative technique of extracting velocity data from a desired flow region. It was initially photographically based (Adrian and Yao 1983), but has since been implemented digitally (digital PIV or DPIV) using charge-coupled device (CCD) cameras and digital data acquisition and image processing systems (Willert and Gharib 1991, Westerweel 1993). DPIV has flourished and evolved, producing countless variations of implementation such as digital particle tracking velocimetry (DPTV) and stereo DPIV (Adrian 1986, 1991, Arroyo and Greated 1991, Cowen and Monismith 1997, Willert 1997, Raffel *et al* 1998, Webster *et al* 2001), and data processing such as window shifting, and image deformation (Huang 1993a, 1993b, Westerweel *et al* 1997, Nogueira *et al* 2002) that have produced significantly more accurate results.

Emphasis in quantitative flow visualization of fluid mechanics has currently shifted towards volumetric methods. An evolution of DPTV is three-dimensional digital particle tracking velocimetry (3DDPTV). In order to obtain depth information, at least three CCD cameras must be simultaneously synchronized for image acquisition, and placed at optimum angles and distances about the test facility. Triangulation schemes are utilized to locate tracer particles upon image acquisition and follow individual particles to obtain velocity vectors (Murai *et al* 1980, Virant and Dracos 1997). The disadvantage of this technique is a compromise between spatial resolution and ambiguities in particle identification due to large tracer particle densities that can only be mitigated with the use of extra cameras. Furthermore, the triangulation schemes employed require laborious calibration of all the cameras (Murai *et al* 1980).

A second volumetric method is holographic particle image velocimetry (HPIV) where holographic pictures are recorded and DPIV methods are used to interrogate successive two-dimensional planes within the hologram. Velocity fields in the planes are then reconstructed into full three-dimensional velocity fields (Barnheart *et al* 1994, Zimin *et al* 1993, Meng and Hussain 1995, Zhang *et al* 1997). This method has proven to be the most promising among the volumetric methods, providing as many as 818 583 velocity vectors distributed through a $97 \times 97 \times 87$ equally spaced grid (Zhang *et al* 1997). However, its complex optical set-up and sensitivity to environmental disturbances makes the usage of this technique awkward. Also, each hologram takes a total of 129 h (five 24 h days, or thirteen 10 h days) to completely process using one processor of an SGI Power Challenger (Zhang *et al* 1997), and this technique can only provide a single snapshot of the flow.

The most recent three-dimensional method to be instituted is the defocusing digital particle image velocimetry (DDPIV), which is capable of minimizing the aforementioned limitations (Pereira *et al* 2000). The foundation of this measurement system was first established by Willert and Gharib (1992) (herein referred to as WG). This technique utilizes a defocusing or blurring concept to obtain information regarding a particle's position in space. This system, differing from the 3DDPTV technique, has one axis common to all associated optics, and uses three-dimensional spatial cross-correlation to obtain the average shift of particles within a voxel (an interrogation volume element). Velocity uncertainties are within 1% of the maximum in the plane perpendicular to the optical axis, and 4 to 6% in the plane parallel to the optical axis. This technique has already been used to map the bubbly flow field about a propeller (Pereira *et al* 2000), and may potentially be used to study transient phenomena and time-averaged statistical behaviour due to the system's ability to acquire sequences of images.

In order to implement the DDPIV volumetric technique, efforts must be made to characterize the geometry of the system through mathematical expressions. A significant contribution to the mathematical description of DDPIV has been pioneered by Pereira *et al* (2000) (herein referred to as PGDM) and expanded upon by Pereira and Gharib (2002) (herein referred to as PG). The equations that have been derived are appropriate only for a two-dimensional optical arrangement, and have been subsequently used to describe a three-dimensional optical arrangement. Hence, these equations do not accurately describe the full three-dimensional nature of this measurement method.

It is therefore the purpose of this paper to present a set of modified equations that can properly describe the DDPIV system in three dimensions. In section 2, the principle of the DDPIV system will be revisited, and previous implementations of this principle by PGDM and PG will be reviewed. This will then set the foundation for which the present full three-dimensional description of the DDPIV will be presented and described in section 3. A geometric uncertainty analysis for the full three-dimensional description of the DDPIV is derived in section 4, where a comparative foundation of the present DDPIV with PG will be established. Finally, in section 5, a juxtaposition of the present derivation with the previous derivations of PGDM and PG is discussed in detail.
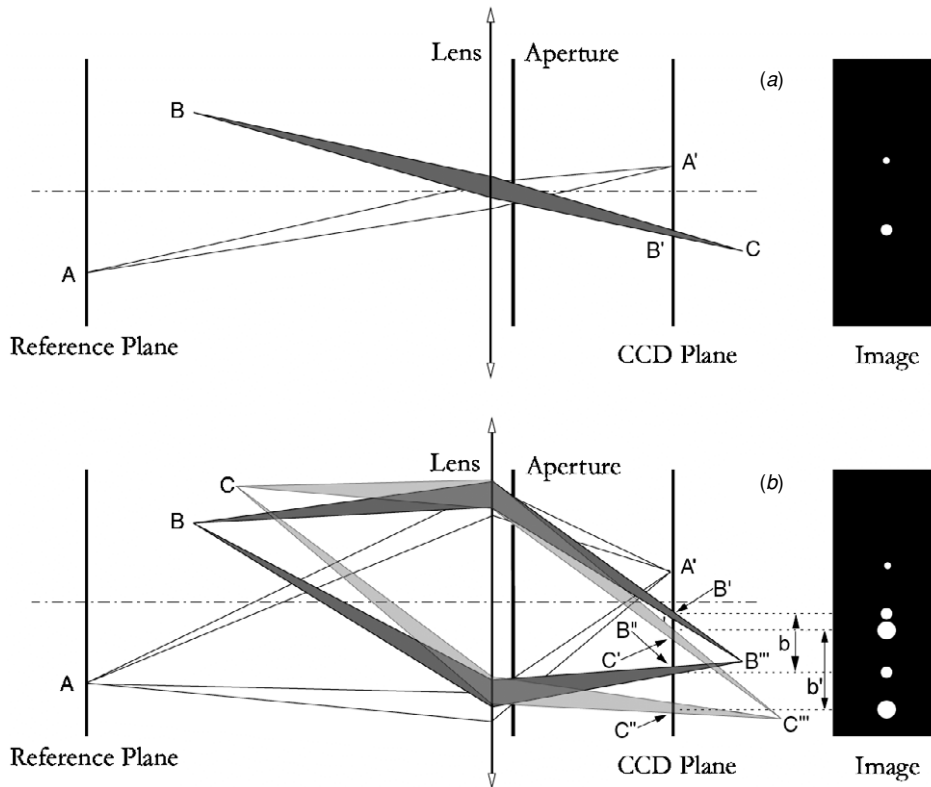
Figure 1. (*a*) Defocusing concept graphically demonstrated: a standard imaging set-up with aperture on-axis; (*b*) defocusing set-up with two off-axis apertures. Point A focuses from the reference plane onto the CCD plane; point B focuses behind the CCD plane at point B‴, leaving two slightly blurred images on the CCD plane (B′ and B″) at a distance *b* apart; point C focuses further behind the CCD plane at point C‴, leaving two slightly larger blurred images on the CCD plane (C′ and C″) at a larger distance *b*′ apart (adapted from Willert and Gharib (1992) and Pereira and Gharib (2002)).

2. Defocusing digital particle image velocimetry: previous geometric analysis and limitations

2.1. Principle

The principle behind the DDPIV system is best described by using a two-dimensional representation of the imaging system shown in figure 1. In figure 1(*a*), rays from a particle located at A focus onto point A′ on the CCD plane. Rays from a particle located at B (off the reference plane), while still travelling through the aperture, focus away from the CCD plane onto point C, leaving a blurred image, B′, on the CCD plane. Note that in this configuration, it is not possible to obtain information about a particle's depth location.

However, by taking advantage of the blurring principle just described, one can modify the aperture in order to obtain full information about a particle's position in space. In figure 1(*b*), the aperture is replaced with two apertures that are at off-axis locations. In this configuration, rays from a particle located at A, though travelling through both apertures, are still focused onto A′. Similarly, rays from point B focus off the CCD plane, onto B‴. However, because the apertures are off-axis, while converging onto point B‴, the rays leave two blurred spots on the CCD plane, B′ and B″, separated by a distance *b*. If a particle located at B were to move farther from the reference plane to C, rays from this particle would focus off the CCD plane, onto C‴, leaving two blurred spots

on the CCD plane, C′ and C″, separated by a distance *b*′ that is larger than *b*. Consequently, this geometry shows that the particle image separation on the CCD plane gets larger as the particle moves farther away from the reference plane, thus providing a way to gauge the depth location. A particle's location orthogonal to the optical axis can also be determined by gauging the displacement of the particle image centre from the optical axis. In this manner, the location of a particle in space can be fully determined.

2.2. Previous geometric analysis

As derived by WG and used by PGDM and PG, using the two-dimensional diagrams shown in figure 1 and geometric ray tracing, a particle's position is shown to be

$$Y = \frac{-y_0 Z(L-f)}{fL} = \frac{-y_0 Z}{ML}, \qquad y_0 = \frac{y' + y''}{2} \qquad (1a)$$

$$X = \frac{-x_0 Z(L-f)}{fL} = \frac{-x_0 Z}{ML}, \qquad x_0 = \frac{x' + x''}{2} \qquad (1b)$$

$$Z = \frac{1}{\frac{1}{L} + Kb}, \qquad (1c)$$

$$K = \frac{1}{MLd}, \qquad b = \frac{Md}{Z}(L-Z), \qquad M = \frac{f}{L-f}, \qquad (1d)$$
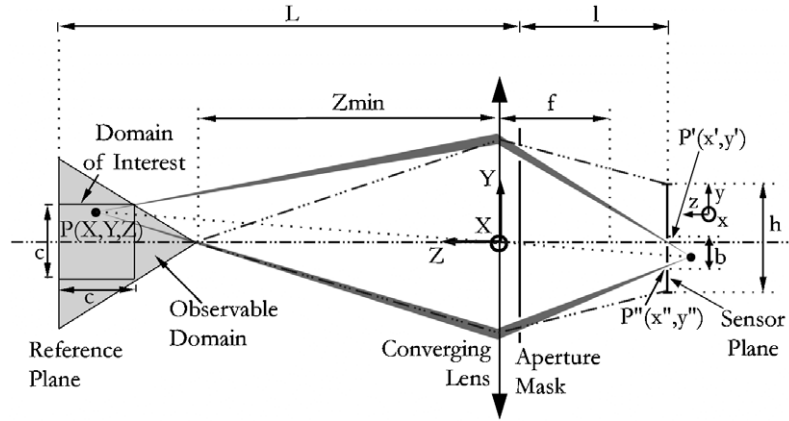
Figure 2. Representation of a pseudo-three-dimensional defocusing optical layout with a cubic domain of interest as represented by PGDM and PG (adapted from Pereira and Gharib (2002)).

where M is the geometric magnification, d is the distance between the centres of the apertures, L is the distance from the aperture plane to the reference plane, (X, Y, Z) are the coordinates of a point in space not on the reference plane (i.e. point B or point C), (x_1', y_1') and (x_2', y_2') are the blurred images on the CCD plane (i.e. points B$'$ and B$''$ or points C$'$ and C$''$) on the CCD plane and b is the separation distance between the blurred images on the CCD plane. The sensitivity of this system to detect changes in the depth location of a particle is given by

$$\frac{\partial b}{\partial Z} = -\frac{1}{KZ^2}. \qquad (2)$$

While there are no bounds on this function, the region between the lens and the reference plane demonstrates better sensitivity (i.e. larger values of this function) than the region beyond the reference plane, suggesting that this region should be used to image the volume of interest. In addition, another way to increase the system sensitivity is to minimize the gain factor, K.

Further analysis by PG has identified the observable domain by the DDPIV system, shown in light grey in figure 2. While seen as a two-dimensional triangle in this figure, this region is in fact a volume within which the DDPIV system is able to image particles, and thereby obtain their positions in space. On the Z-axis, this observable domain exists within the reference plane located at L, and the apex of this triangular region is located at Z_{min}. Furthermore, a design constraint defined as the 'domain of interest' has been introduced that defines the largest cubic domain of side c that can exist within the observable domain. The location of Z_{min}, expressed as a function of the dimension of the domain of interest c, is given as

$$Z_{min} = \frac{d(L-c)}{d+c}. \qquad (3)$$

As pointed out by WG, using a two-pinhole mask to image densely seeded flows presented the difficulty of uniquely matching particle image pairs, which resulted in ambiguous data. To overcome this ambiguity problem, a three-pinhole mask, where the pinholes were placed at the vertices of an equilateral triangle, was suggested and used (see figure 3). With this configuration, the CCD sensor was triply exposed, such that the pinhole exposures were also located at the
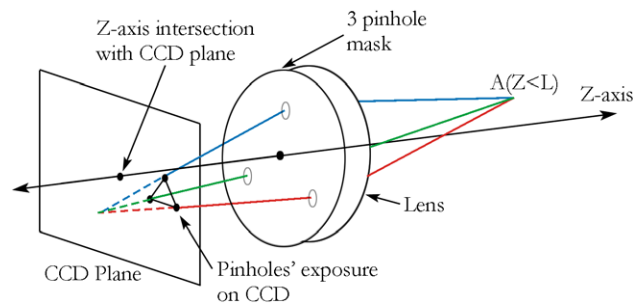

Figure 3. DDPIV using a three-pinhole mask (adapted from Pereira *et al* (2000)).

vertices of an equilateral triangle. While the three-pinhole mask did overcome the ambiguity problem, there were still two other problems that remained. First, since each particle now produced triple exposures onto the CCD sensor, imaging heavily seeded flows resulted in heavily overlapped particle images, hence making particle identification extremely difficult. Second, for optimal experimental configurations, the pinhole separations were required to be of the order of the dimension of the domain of interest, c. This necessitated that the lens also be at least of the same dimension, thereby posing a problem as obtaining custom-made large lenses could be quite costly.

The solution was to redesign the DDPIV camera to use three separate imaging systems, each located at a specific distance from a common axis (see figure 4). To insure that each of the three systems would image the same reference area, each CCD sensor was appropriately displaced laterally from the local optical axis of their respective lens. This allowed a common reference area from the reference plane to be imaged onto each of the three CCD sensors. This new set-up then allowed each of the triple particle images to be exposed onto a separate CCD sensor, hence preventing the overcrowding problem. Furthermore, off-the-shelf optics could now be used to construct the DDPIV camera, negating the need to invest in costly custom-built large lenses. In functionality, this new design is equivalent to the single lens design discussed above and shown in figure 3 (Gharib *et al* 1998). It can be seen in figure 4, for example, that a particle located at A produces an image towards the upper left corner in CCD 1, an
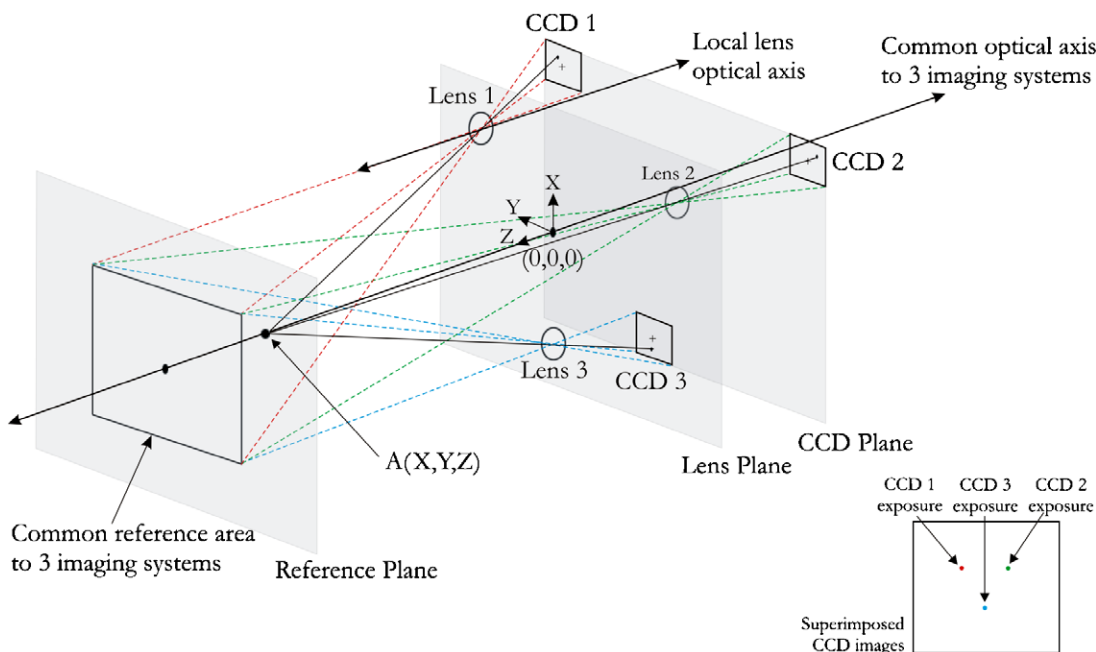
Figure 4. Implementation of 3D defocusing PIV allowing for the use of off-the-shelf hardware items.

image towards the upper right corner in CCD 2 and an image towards the bottom side in CCD 3. When these images are superimposed, the triple exposure in the form of an equilateral triangle is regained.

2.3. Limitations

While all the modifications discussed above have been able to improve the DDPIV hardware's ability to image particles, the geometric analysis that describes this system has still remained the same, and has not been changed to reflect the hardware modifications. To understand why such a change is necessary, it is important to note that the two-dimensional derivation requires the two pinholes to be off-axis in the Y–Z plane and on-axis in the X–Z plane (see figure 2), allowing for the derivation of equation ($1a$). Similarly, when an analysis is done with two pinholes off-axis in the X–Z plane and on-axis in the Y–Z plane, equation ($1b$) is derived. This is best seen by studying figure 5, which is a three-dimensional view of the two-dimensional optical set-up shown in figure 2. In figure 5, a particle located at point A, which is not on the reference plane, is imaged through a four-pinhole mask onto point A'. The four pinholes are located on the mask such that two pinholes are placed on the extremes of the lens' vertical diameter, while the other two pinholes are placed on the extremes of the lens' horizontal diameter. For clarity, the rays passing through the pinholes on the lens' vertical diameter are shown to be within the 'vertical plane', while the rays passing through the pinholes on the lens' horizontal diameter are shown to be within the 'horizontal plane'. Both of these planes, though tilted with respect to the optical axis, remain flat and unbent. This pinhole arrangement, as shown by the ray tracing, results in the exposure of four particle images on the CCD plane, located at (x_0, y'), (x_0, y''), (x', y_0) and (x'', y_0), where the centre of these points is located at (x_0, y_0). This figure therefore shows that figures $1(b)$ and 2 are the projection of the vertical plane and its associated rays

and vertically placed CCD pinhole exposures onto the Y–Z plane. Thus, within this projection onto the Y–Z plane, the location of point A as a function of the exposure points, (x_0, y') and (x_0, y''), is described by equations ($1a$), ($1c$) and ($1d$). Likewise, when the horizontal plane and its associated rays and horizontally placed CCD pinhole exposures are projected onto the X–Z plane, the location of point A within the X–Z plane as a function of the exposure points, (x', y_0) and (x'', y_0), is described by equations ($1b$), ($1c$) and ($1d$).

While equations (1) can properly identify a particle image's location if the pinholes are located on the lens' diameter as shown in figure 5, they cannot accurately predict a particle's location if the pinholes are located off the diameter of the lens. This is best seen by studying figure 6. Two pinholes, shown by the open circles, are used to demonstrate the geometric optics for pinholes that are located on the lens' vertical diameter, as previously shown in figure 5. In addition, three pinholes, each located at the vertex of an equilateral triangle, are shown by open stars. For ease of comparison, the star-shaped pinholes are situated such that two of the three pinholes are located on a vertical chord of the lens. Rays emanating from point A pass through the pinholes on the lens' vertical diameter, and are refocused towards A', leaving two exposure points on the CCD plane, denoted by the solid circles. Likewise, rays emanating from point A also pass through the pinholes designated by the open stars (rays passing only through the two pinholes that lie on the vertical chord of the lens are shown), and are refocused towards A', leaving two exposure points on the CCD plane, denoted by the solid stars. While the distance in the y-direction between the two solid circles and the distance between the two solid stars seem identical, the distance of the solid circles from the y-axis in the x-direction is noticeably different from the distance of the solid stars from the y-axis in the x-direction. This observation clearly indicates that equations (1) cannot be used to accurately determine the position of a particle in space if the pinholes are
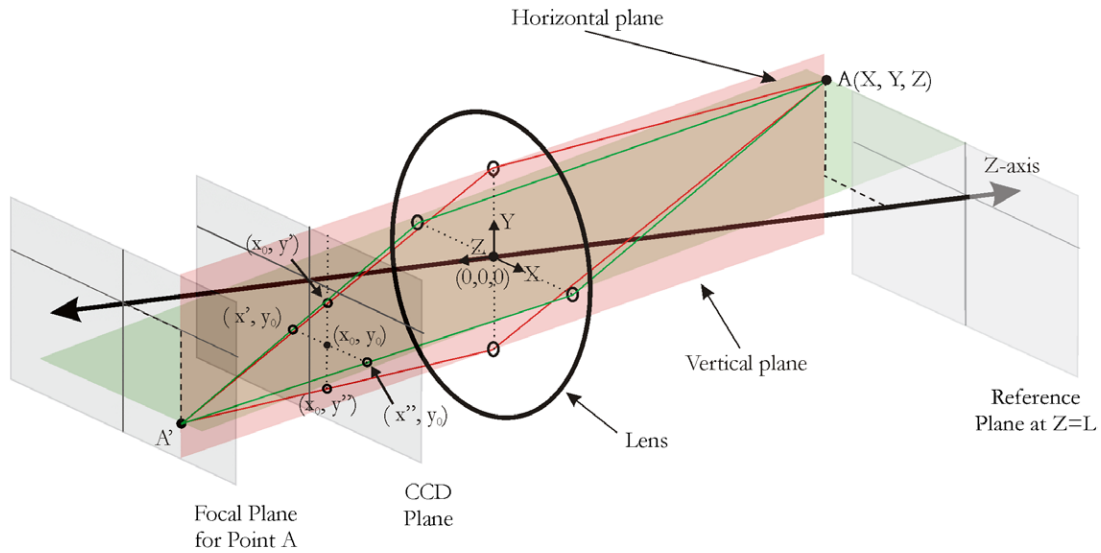
Figure 5. Application of two-dimensional equations (see equations (1)) to a full three-dimensional DDPIV system.
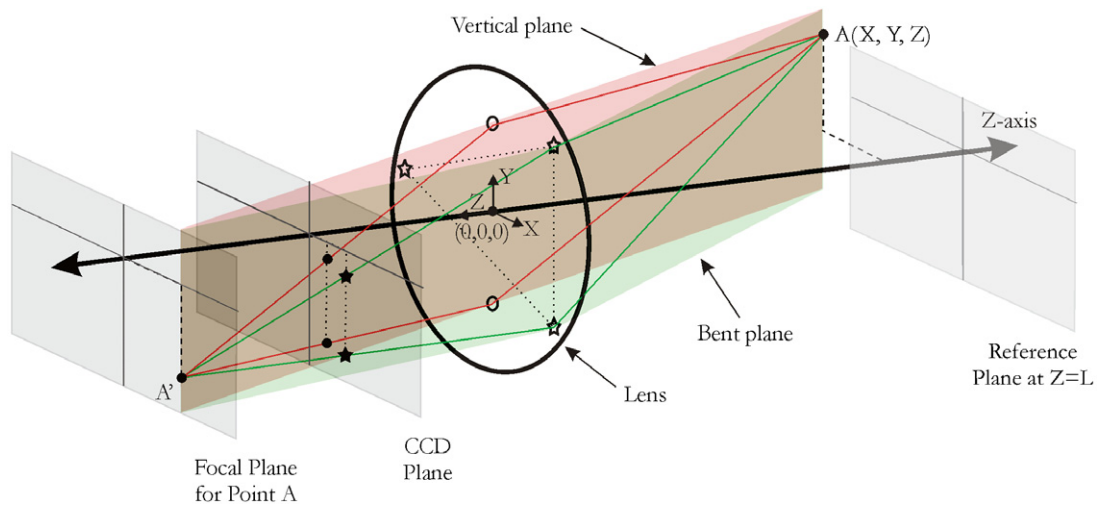

Figure 6. Comparison of imaging effects using an on-axis two-pinhole mask and an off-axis three-pinhole mask.

located off the lens' diameter, and that a full three-dimensional derivation is required for such an accurate determination.

3. Defocusing digital particle image velocimetry—a three-dimensional geometric analysis

3.1. Derivation assumption

The derivations presented in this paper assume that the lenses to be used in the optical system will be thin, and the F number of the lenses defined as

$$F = \frac{f}{D}, \tag{4}$$

where f is the focal length of the lens and D is its diameter, will be large to minimize the effects of spherical aberrations that could lead to the distortion of the triangles imaged on the CCD sensor. This assumption is important as it leads to the validity of utilizing equations such as the general thin lens equation within the derivations. The effects of spherical aberrations become particularly noticeable at the edges of images for low

F number lenses. This is an important detail to be mindful of in the design phase when selecting appropriate lenses for the DDPIV camera system.

3.2. Volume of interest

A simplified representation of the DDPIV system, including the viewing cones of each of the CCD sensors, is shown in figure 7. The volume where all three viewing cones intersect defines the 'observable domain'. The location where all three viewing cones intersect at a point is identified as Z_{min}, which defines the closest point to the lens plane in which a particle can be identified in space. A plane cut in between the reference plane and Z_{min} is extracted and shown in figure 8. The light grey shows the areas seen by each CCD sensor, the medium grey shows the areas seen by two CCD sensors, and the dark grey shows the area seen by all three CCD sensors. While the sides of the observable domain have an associated radius of curvature, for the purposes of analysis, a second contour may be redefined by introducing the imbedded inverted equilateral
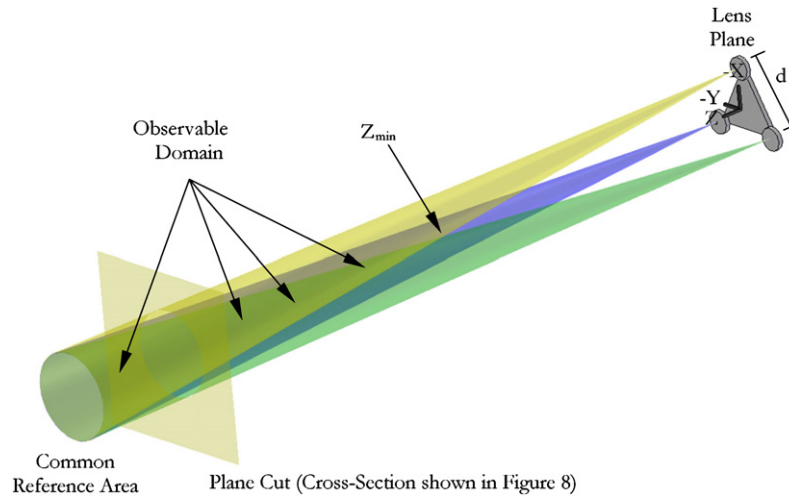
Figure 7. Three-dimensional defocusing arrangement upon which the full three-dimensional equations are derived.
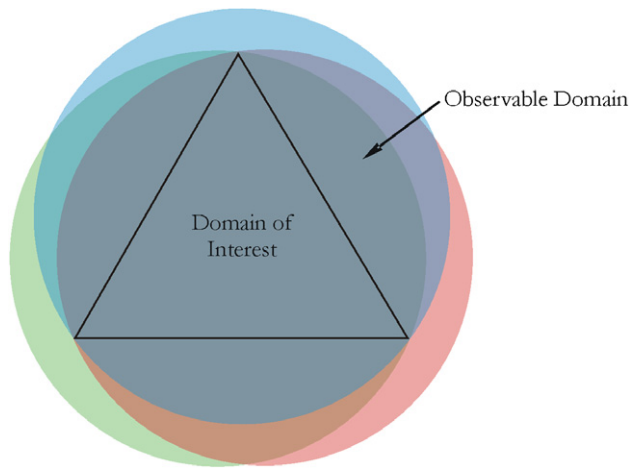

Figure 8. Inscribed domain of interest in the mutually observed region of all three lenses. (The cross-section of the plane cut is shown in figure 7.)

triangle. This second contour, which now subsections a cross-section of the 'domain of interest' within the observable domain, is a favourable one because of its ability to uniquely and completely express the geometric parameters of the system using equations exclusively, with fewer inputs than required in previous derivations. It is important to note that even though the cross-section of the domain of interest is approximated by a triangular cross-section, the cameras will have the ability to capture the particle images outside the domain of interest, though within the observable domain. Conceptually then, the complete domain of interest extends from Z_{min} back to the reference plane and can be characterized as a tetrahedron, with the cross-sectional area increasing with distance away from the optical origin. The domain of interest, however, will not include the reference plane since particles imaged from this plane onto the CCD sensors result in exposures that are located at identical locations on the three sensors, and therefore full three-dimensional spatial information of the imaged particle will not be identifiable (see PGDM and PG). From this complete domain of interest, only a segment of finite thickness is selected to be imaged (see figure 9). Therefore,

the 'volume of interest' may be uniquely defined by three parameters: side-length of the front-face, a_{pf}, side-length of the back-face a_{pb}, and the thickness of the volume, a_z. Due to convention and geometric arguments, a_{pb} must be larger than a_{pf}. Figure 10 depicts the cross-sectional view of the front and rear faces of the volume of interest. It will be shown that the geometric parameters of the system are dependent primarily upon the side-lengths of the front and rear faces of the volume under analysis.

It is also important to note that from geometry, the vertices of the equilateral triangle are all equidistant from the optical axis. There are important consequences in having the domain of interest positioned in this orientation. Namely, the projection of the three-dimensional optical geometry onto the X–Z and Y–Z planes would result in different distances of the lenses from the optical axis as shown in figures 11 and 12, respectively. The asymmetrical lens distances in the X–Z plane shown in figure 11 must be taken into account in the full three-dimensional derivations characterizing the geometry of the DDPIV camera system. As a result, equations will no longer be strictly a function of the side-length lens difference, d, but also of γ, the radial distance of the lenses from the optical axis (shown in figure 11).

From the geometric descriptors of the volume of interest, the location of Z_{min} relative to the optical origin is

$$Z_{min} = Z_a + a_z \left(\frac{a_{pf}}{a_{pf} - a_{pb}} \right), \tag{5}$$

where Z_a is defined to be the location of the front face of the volume of interest relative to the lenses plane (optical origin). The parameter, d, a derived quantity in the full three-dimensional derivation, is determined to be

$$d = \frac{Z_a(a_{pb} - a_{pf}) - a_z a_{pf}}{a_z}. \tag{6}$$

This is a very significant result because the lens separation distance is now completely defined by the location and dimensions of the volume of interest, whereas previous derivations required this to be an input parameter.
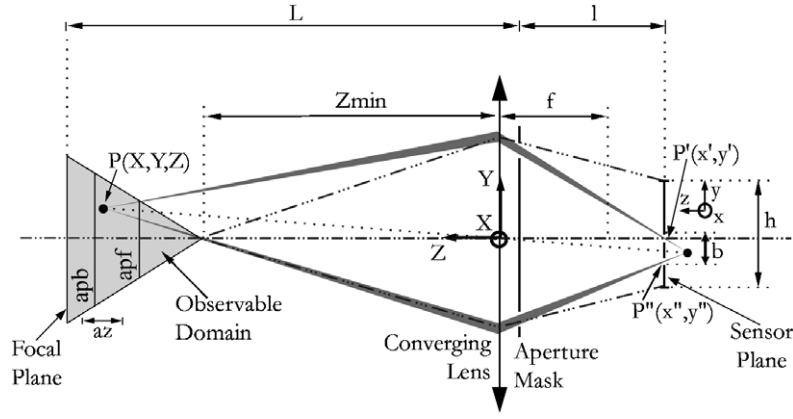
Figure 9. Two-dimensional projection of a three-dimensional defocusing optical model with a new domain of interest.
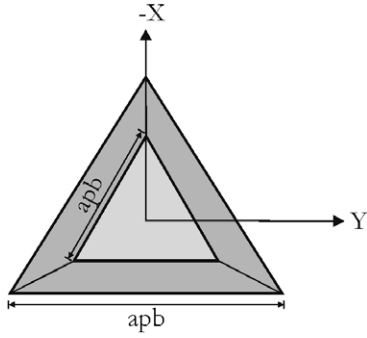

Figure 10. Volume of interest in the full three-dimensional derivation.

3.3. Image coordinates

When the optics and the CCDs are placed around the optical axis at the vertices of an inverted equilateral triangle, the triple exposure is also in the form of an equilateral triangle (see figure 4). The coordinates of these exposure points, (x_B, y_B), (x_{TL}, y_{TL}) and (x_{TR}, y_{TR}), referenced in figure 13, are defined by a fixed axis centred on each of the three CCD sensors and are superimposed onto a single plane to generate an equilateral triangle. The abscissa and ordinate of the coordinate system in figure 13 are represented in this way to be consistent with

the coordinate systems of figures 4, 5, 7, 9, 10, 11 and 12. These three pairs of image coordinates collectively define the projection of particles located at the space coordinates (X, Y, Z) as follows:

$$x_B = -\frac{M}{Z}[XL + \gamma(L - Z)] + \frac{2 - \sqrt{3}}{2\sqrt{3}}h \qquad (7a)$$

$$x_{TR} = x_{TL} = -\frac{M}{2Z}[2LX - \gamma(L - Z)] + \frac{2 - \sqrt{3}}{2\sqrt{3}}h \quad (7b)$$

$$y_B = -\frac{Yl}{Z} \qquad (7c)$$

$$y_{TR} = \frac{M}{2Z}[-d(L - Z) - 2LY] \qquad (7d)$$

$$y_{TL} = \frac{M}{2Z}[d(L - Z) - 2LY], \qquad (7e)$$

where the parameter γ, shown in figure 11, is the radial distance from the optical Z-axis to the lenses (it can also be shown from geometry that $\gamma = d/\sqrt{3}$), l is the distance between the lenses and sensors along the optical axis, h is the height or size of the CCD sensor, and M is the magnification as defined below:

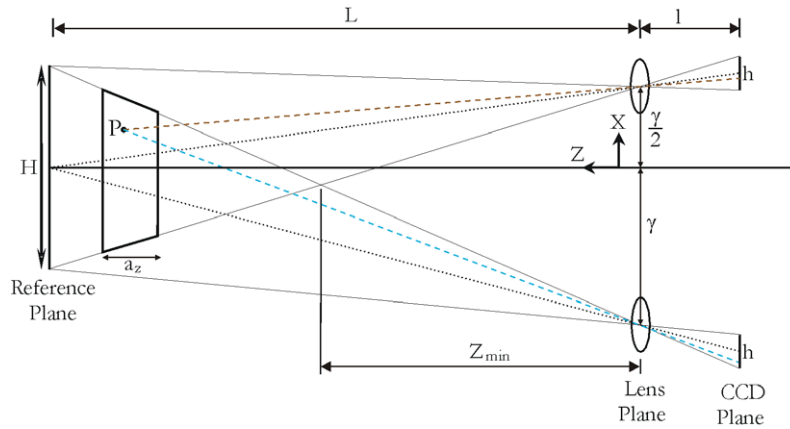$$M = \frac{f}{L - f} = \frac{hZ_{min}}{d(L - Z_{min})}. \qquad (8)$$

Figure 11. X–Z projection of the three-dimensional DDPIV camera system.
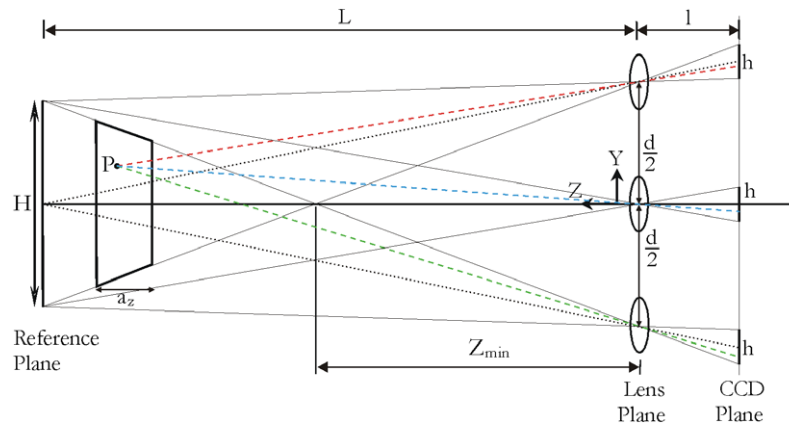
Figure 12. *Y–Z* projection of the three-dimensional DDPIV camera system.
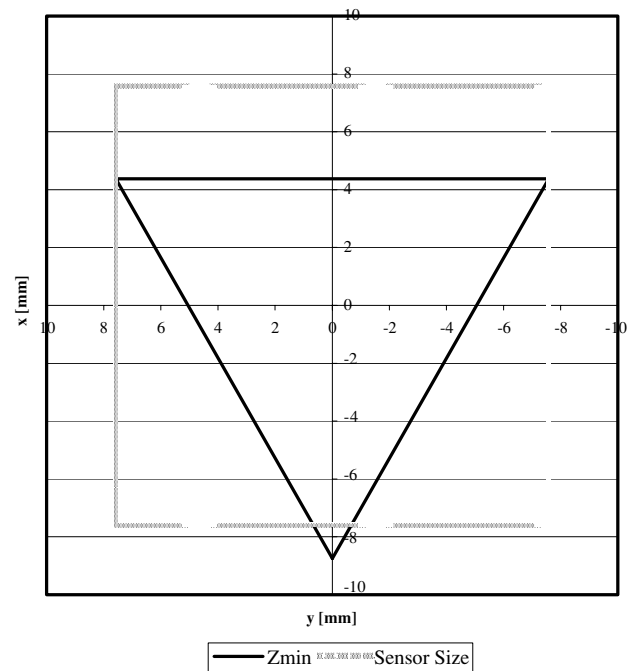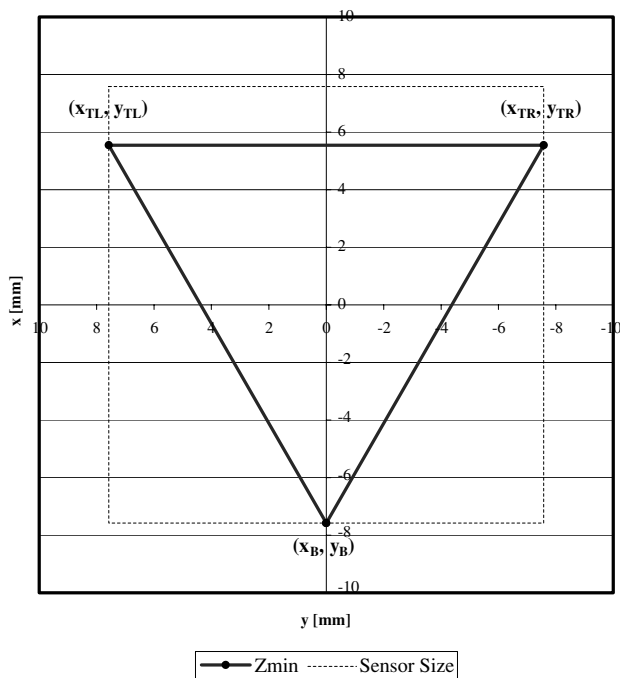

Figure 13. An imaged particle on a superimposed sensor plane located on the optical axis at Z_{min}.

Figure 14. Superposition of the projection of particles onto the CCD sensors without the compensating shift term.

These expressions for the image coordinates were derived under the stipulation that at Z_{min} the largest possible triangular image should be mapped onto the CCD sensor. Therefore, the side-length of the axisymmetric, equilateral triangle mapped onto the CCD sensor at Z_{min} is optimized to be the physical size of the CCD sensor, h. While this condition is necessary to satisfy this stipulation, it is not sufficient. Figure 14 shows that while the triangle side-length is optimized to the sensor size, its location is not, as the lower portion of the triangle lies outside the sensor area (Ponchaut *et al* 2004). To accommodate for this, all three CCD sensors are shifted down by an equivalent amount, as indicated by the last terms of equations (7*a*) and (7*b*). With these shifting terms, the entire image, including a particle located on the optical axis at Z_{min}, can be completely mapped onto the CCD sensor as seen in figure 15. Note that these shifting terms are independent of magnification and are constant for a given CCD sensor. The large triangle,

therefore, represents a point located on the optical Z-axis at Z_{min}. The three smaller triangles located at the vertices of the large triangle correspond to points located at the vertices of the triangular cross-section of the front face of the volume of interest (see figure 10). The significance of these triangles is that they clearly demonstrate that every point within the volume of interest in real space, including its boundary and the back face, can be imaged onto a CCD sensor within this large triangle. The projection of the points located at the vertices of the triangular cross-section of the back face of the volume of interest would look similar to figure 15; only the three corner triangles would have a smaller side-length, b, as the Z-axis location of such particles will be closer to the reference plane. For completeness, a triangle in the centre of the optimized Z_{min} triangle was added, representing a particle located on the front face of the domain of interest on the optical axis.
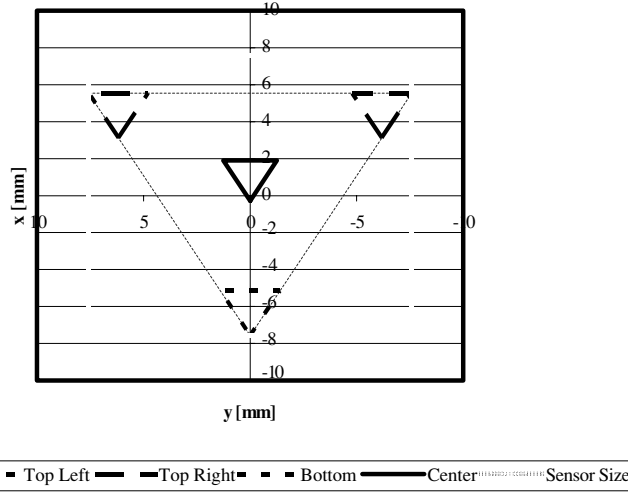
Figure 15. Superposition of the projection of particles, located at the front face of the domain of interest, onto the CCD sensors with the compensating shift term.

Finally, solving equations (7) for the space coordinates (X, Y, Z) as a function of the three-particle image coordinates gives

$$X = \frac{1}{2L}\left(\frac{-2Zx_{\mathrm{TL}}}{M} + \gamma(L-Z)\right)$$
$$= \frac{1}{2L}\left(\frac{-2Zx_{\mathrm{TR}}}{M} + \gamma(L-Z)\right)$$
$$= \frac{1}{L}\left(\frac{-Zx_{\mathrm{B}}}{M} - \gamma(L-Z)\right), \quad (9a)$$

which simplifies to

$$X = \frac{-x_0 Z}{ML}, \qquad x_0 = \frac{x_{\mathrm{TR}} + x_{\mathrm{TL}} + x_{\mathrm{B}}}{3}, \quad (9b)$$

$$Y = \frac{1}{2L}\left(-\frac{2Zy_{\mathrm{TL}}}{M} + d(L-Z)\right)$$
$$= -\frac{1}{2L}\left(-\frac{2Zy_{\mathrm{TR}}}{M} - d(L-Z)\right) = -\frac{y_{\mathrm{B}}Z}{l}, \quad (9c)$$

which simplifies to

$$Y = \frac{-y_0 Z}{ML}, \qquad y_0 = \frac{y_{\mathrm{TR}} + y_{\mathrm{TL}} + y_{\mathrm{B}}}{3}, \quad (9d)$$

and

$$Z = \left(\frac{1}{L} + \frac{b}{MdL}\right)^{-1} = \left(\frac{1}{L} + \frac{\zeta}{M\gamma L}\right)^{-1}, \quad (9e)$$

where (x_0, y_0) marks the centre of the equilateral triangle that the particle images identify, and ζ is the distance from the centre of this equilateral triangle to any of the particle's images that identify any vertex of the equilateral triangle (i.e. $(x_{\mathrm{B}}, y_{\mathrm{B}})$, $(x_{\mathrm{TL}}, y_{\mathrm{TL}})$ or $(x_{\mathrm{TR}}, y_{\mathrm{TR}})$).

3.4. Image separation

The image separation, b, characterizes the side-length of the projected triangular image in the superimposed sensor plane (see figure 9). This follows the derivation of the local sensor coordinates, and applying the distance formula for two adjacent vertices of the equilateral triangle yields

$$b = \frac{1}{K}\left|\frac{1}{Z} - \frac{1}{L}\right| \quad (10)$$

where

$$K = \frac{1}{MdL}. \quad (11)$$

Note that at $Z_{\min}$ the length of b is equivalent to the size of the CCD sensor; in other words the ratio between the separation distance and the sensor height is exactly one. This parameter captures the particle's Z-location along the optical axis.

The sensitivity of the system to depth location, established by Willert and Gharib (1992), is based upon the rate of change of b with respect to the distance along the optical axis. The ability of the image separation parameter to discern a small displacement of a particle along the optical axis is expressed in terms of a separation gradient given by

$$\frac{\partial b}{\partial Z} = -\frac{1}{KZ^2}. \quad (12)$$

This term should be minimized (i.e. its magnitude should be maximized) when determining the geometric parameters of the system so that smaller relative uncertainties of particle location within the Z-direction (depth) can be obtained.

4. Error analysis

Given the expressions for a particle's image positions on the CCD sensors as a function of the particle's spatial coordinates (see equations (7)), a particle's image displacement as a function of the particle's spatial displacement can be obtained by differentiation (Lawson and Wu 1997):

$$\mathrm{d}x_{\mathrm{B}} = \frac{\partial x_{\mathrm{B}}}{\partial X}\mathrm{d}X + \frac{\partial x_{\mathrm{B}}}{\partial Y}\mathrm{d}Y + \frac{\partial x_{\mathrm{B}}}{\partial Z}\mathrm{d}Z$$

$$\mathrm{d}y_{\mathrm{B}} = \frac{\partial y_{\mathrm{B}}}{\partial X}\mathrm{d}X + \frac{\partial y_{\mathrm{B}}}{\partial Y}\mathrm{d}Y + \frac{\partial y_{\mathrm{B}}}{\partial Z}\mathrm{d}Z$$

$$\vdots \qquad\qquad (13)$$

$$\mathrm{d}x_{\mathrm{TL}} = \frac{\partial x_{\mathrm{TL}}}{\partial X}\mathrm{d}X + \frac{\partial x_{\mathrm{TL}}}{\partial Y}\mathrm{d}Y + \frac{\partial x_{\mathrm{TL}}}{\partial Z}\mathrm{d}Z$$

where $\{\mathrm{d}X, \mathrm{d}Y, \mathrm{d}Z\}$ are the displacements in the space coordinates, and $\{\mathrm{d}x_{\mathrm{B}}, \mathrm{d}y_{\mathrm{B}}, \mathrm{d}x_{\mathrm{TR}}, \mathrm{d}y_{\mathrm{TR}}, \mathrm{d}x_{\mathrm{TL}}, \mathrm{d}y_{\mathrm{TL}}\}$ are the displacements in the local image coordinates. By evaluating

the partial derivatives, these equations can be expressed in matrix form for simplicity,

$$\begin{Bmatrix} dx_B \\ dy_B \\ dx_{TR} \\ dy_{TR} \\ dx_{TL} \\ dy_{TL} \end{Bmatrix} = \begin{bmatrix} A & 0 & B \\ 0 & A & C \\ A & 0 & D \\ 0 & A & E \\ A & 0 & D \\ 0 & A & F \end{bmatrix} \begin{Bmatrix} dX \\ dY \\ dZ \end{Bmatrix}, \qquad (14)$$

where

$$A = -\frac{ML}{Z}, \qquad B = \frac{M\gamma L}{Z^2} + \frac{MXL}{Z^2}, \qquad C = \frac{YLM}{Z^2},$$

$$D = -\frac{M\gamma L}{2Z^2} + \frac{MXL}{Z^2},$$

$$E = \frac{MdL}{2Z^2} + \frac{MYL}{Z^2}, \qquad F = -\frac{MdL}{2Z^2} + \frac{MYL}{Z^2}. \qquad (15)$$

Since the present derivation is focused on determining the measurement uncertainties due to the camera design and geometry, the uncertainties due to h, d, l, f, L and γ are neglected. Furthermore, it can also be assumed that the uncertainties in the image plane are equal such that

$$\delta(dx_B) = \delta(dx_{TR}) = \delta(dx_{TL}) = \delta(dy_B)$$
$$= \delta(dy_{TR}) = \delta(dy_{TL}) = \Delta x. \qquad (16)$$

Inverting equation (13) results in

$$\begin{Bmatrix} dX \\ dY \\ dZ \end{Bmatrix} = \begin{bmatrix} A' & 0 & B' & C' & B' & -C' \\ -2D' & E' & D & F' & D' & G' \\ -2H' & 0 & H' & -I' & H' & I' \end{bmatrix} \begin{Bmatrix} dx_B \\ dy_B \\ dx_{TR} \\ dy_{TR} \\ dx_{TL} \\ dy_{TL} \end{Bmatrix}, \qquad (17)$$

where

$$A' = \frac{-Z}{3LM}\left(\frac{d^2 + 3\gamma(\gamma - 2X)}{d^2 + 3\gamma^2}\right),$$

$$B' = \frac{-Z}{3LM}\left(\frac{d^2 + 3\gamma(\gamma + 3X)}{d^2 + 3\gamma^2}\right),$$

$$C' = \frac{-ZXd}{LM}\left(\frac{1}{d^2 + 3\gamma^2}\right),$$

$$D' = \frac{-YZ\gamma}{LM}\left(\frac{1}{d^2 + 3\gamma^2}\right), \qquad E' = \frac{-Z}{3LM}, \qquad (18)$$

$$F' = \frac{-Z}{3LM}\left(\frac{d^2 + 3\gamma(\gamma + 3Y)}{d^2 + 3\gamma^2}\right),$$

$$G' = \frac{-Z}{3LM}\left(\frac{d^2 + 3\gamma\left(\gamma - \frac{Yd}{\gamma}\right)}{d^2 + 3\gamma^2}\right),$$

$$H' = \frac{-\gamma Z^2}{LM}\left(\frac{1}{d^2 + 3\gamma^2}\right), \qquad I' = \frac{dZ^2}{LM}\left(\frac{1}{d^2 + 3\gamma^2}\right).$$

Using standard error analysis, the uncertainties on a particle's displacement in space coordinates are:

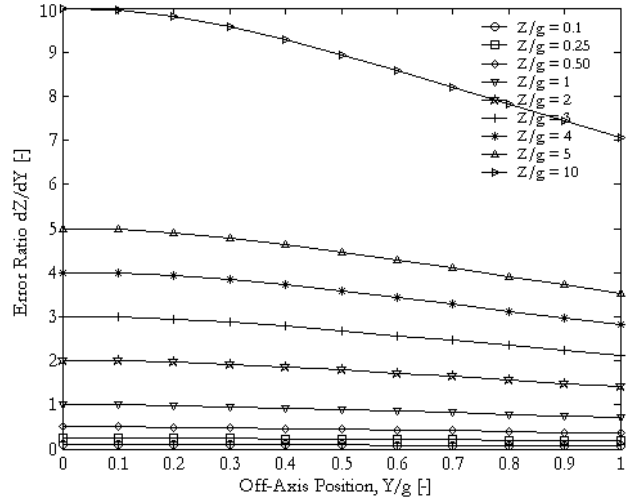$$\delta(dX) = \frac{\Delta x}{\sqrt{3}}\frac{|Z|}{ML}\sqrt{1 + \frac{X^2}{\gamma^2}} \qquad (19a)$$

Figure 16. Error ratio $\frac{\delta(dZ)}{\delta(dY)}$ versus the off-axis position, $\frac{Y}{\gamma}$, for various distances to the camera, $\frac{Z}{\gamma}$. Here, g represents γ.

$$\delta(dY) = \frac{\Delta x}{\sqrt{3}}\frac{|Z|}{ML}\sqrt{1 + \frac{Y^2}{\gamma^2}} \qquad (19b)$$

$$\delta(dZ) = \frac{Z^2}{MdL}\Delta x = KZ^2\Delta x. \qquad (19c)$$

Similarly, using equation (12), the uncertainty of the separation parameter, b, becomes

$$\delta(db) = \Delta x. \qquad (20)$$

Since one of the benefits of the DDPIV system is its ability to provide depth information, a useful parameter that can be used to measure the overall performance of the system is the ratio of the out-of-plane to the in-plane uncertainties:

$$e_{YZ} = \frac{\delta(dZ)}{\delta(dY)} = \frac{(|Z|/\gamma)}{\sqrt{1 + \frac{Y^2}{\gamma^2}}} \qquad (21a)$$

$$e_{XZ} = \frac{\delta(dZ)}{\delta(dX)} = \frac{(|Z|/\gamma)}{\sqrt{1 + \frac{X^2}{\gamma^2}}}. \qquad (21b)$$

From these equations, it can be seen that the uncertainty ratios $\frac{\delta(dZ)}{\delta(dY)}$ and $\frac{\delta(dZ)}{\delta(dX)}$ are a linear function of Z. With respect to the off-axis variables, $\frac{\delta(dZ)}{\delta(dY)}$ is a function of Y only, while $\frac{\delta(dZ)}{\delta(dX)}$ is only a function of X. Also, the uncertainty ratio expressions are identical in form. Interesting to note is that equations (19) and (21) suggest that the proper non-dimensionalization parameter for each of the X, Y and Z coordinates is not d, the lens spacing distance, as has been suggested by PG, but rather γ, the radial distance of the lens from the optical axis. Therefore, variations of $\frac{\delta(dZ)}{\delta(dY)}$ with respect to $\frac{Y}{\gamma}$ and $\frac{Z}{\gamma}$ are shown in figures 16 and 17. For comparison with PG, this ratio is also plotted with respect to $\frac{Y}{d}$ and $\frac{Z}{d}$ in figures 18 and 19. Furthermore, plots of the uncertainty ratio $\frac{\delta(dZ)}{\delta(dX)}$ will not be shown as these plots will be identical to those of $\frac{\delta(dZ)}{\delta(dY)}$. Equation (21a) clearly shows that the uncertainty ratio is maximized when the particle is located on the optical axis ($Y = 0$), as shown in figure 18. Also, for
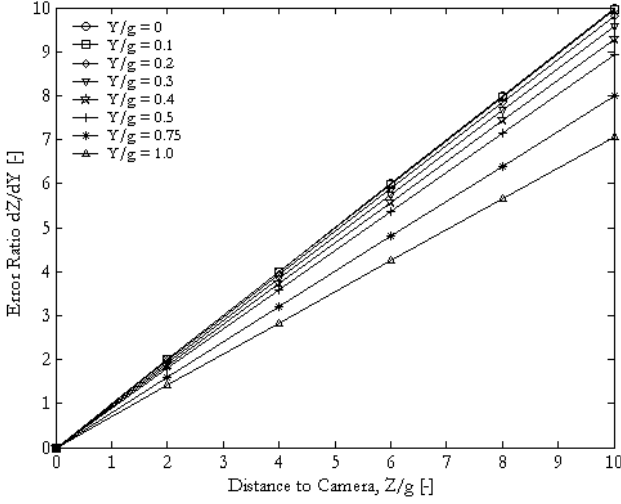
Figure 17. Error ratio $\frac{\delta(dZ)}{\delta(dY)}$ versus distance to camera, $\frac{Z}{\gamma}$, for various off-axis positions, $\frac{Y}{\gamma}$. Here, g represents γ.

Figure 18. Ratio $\frac{\delta(dZ)}{\delta(dY)}$ versus the off-axis position, $\frac{Y}{d}$, for various distances to the camera, $\frac{Z}{d}$.

the various $\frac{Z}{d}$ plots, on the optical axis and on the maximum off-axis locations, the uncertainty ratios are uniformly 13% and 39%, respectively, less than the uncertainty ratio values reported in figure 5 of PG. In figure 19, a plot of $\frac{\delta(dZ)}{\delta(dY)}$ as a function of depth, $\frac{Z}{d}$, for various off-axis distances, $\frac{Y}{d}$, is plotted. For a given off-axis location, the uncertainty ratio is seen to vary linearly with the depth location, Z. As in the previous plot, the uncertainty ratios, on-axis and at the maximum off-axis locations, are similarly seen to be uniformly 13% and 39%, respectively, lower than the corresponding uncertainty ratio given in PG.

5. Discussion

While the equations derived by WG and PGDM and expanded upon by PG were insightful, there remained some ambiguity from extending a two-dimensional derivation to three-dimensional applications resulting from not thoroughly looking into the complete geometry of the system. Below, four areas where the effects of a full three-dimensional derivation
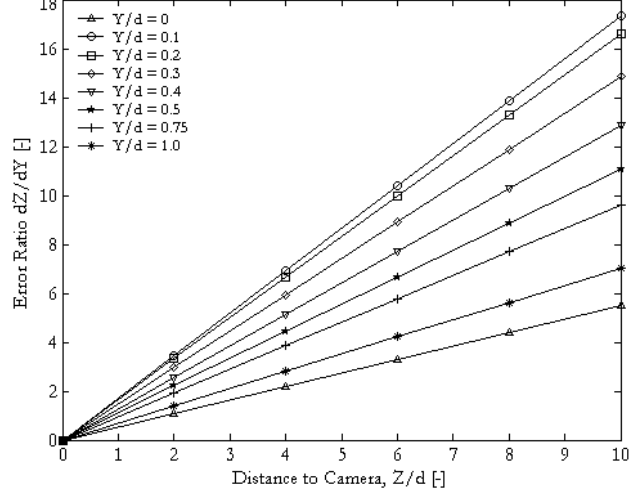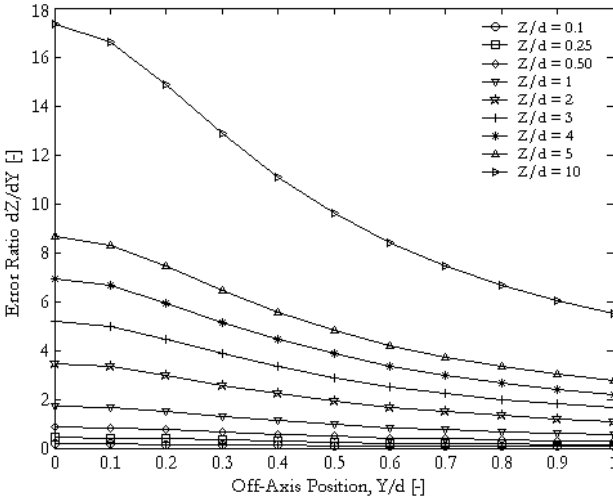

Figure 19. Error ratio $\frac{\delta(dZ)}{\delta(dY)}$ versus distance to camera, $\frac{Z}{d}$, for various off-axis positions, $\frac{Y}{d}$.

Table 1. Comparison between the two-dimensional and the present derivations of the geometric parameters $Z_{\min}$ and d.

	Two-dimensional derivation	Present derivation	Equation
$Z_{\min}$	$\frac{d(L-c)}{c+d}$	$Z_a + a_z \left(\frac{a_{\mathrm{pf}}}{a_{\mathrm{pf}} - a_{\mathrm{pb}}} \right)$	(5)
d	$d > \frac{2L^2}{\frac{k_Z}{k_X} h(L-c) - 2L}$	$\frac{Z_a (a_{\mathrm{pb}} - a_{\mathrm{pf}}) - a_z a_{\mathrm{pf}}}{a_z}$	(6)

are significant are discussed. These include new expressions for the geometric parameters $Z_{\min}$ and d, the effect of the X–Z plane asymmetries on image coordinates, and a discussion of the differences in the expressions utilized in uncertainty analyses and their impact on optimization.

5.1. A comparison of geometric parameters $Z_{\min}$ and d

The first series of equations that introduced a defining distinction between the two derivations are the equations for $Z_{\min}$ and d. Table 1 summarizes the equations in order to compare the derivation by PGDM and PG with the current derivation.

While the two-dimensional derivation is dependent upon the dimensions of a cube, c, that indirectly defines the volume of interest, it is also dependent upon the geometry of the system: distance to the reference plane, L, and the side-length of the lens configuration, d. However, in the present full-three-dimensional derivation, inputs directly define the volume of interest such that $Z_{\min}$ is completely characterized by the location and size of the volume of interest. In other words, $Z_{\min}$ can be determined exclusively by inputs. No further calculations are required (i.e. d and L) to determine its placement with respect to the lens plane. The second distinction is in the lens separation distance, d. In the papers by PGDM and PG, the lens separation distance is a variable input subject to a constraint dependent upon resolution parameters, k_X and k_Z (see table 1). However, in the present derivation, the parameter is completely defined by the location and parameters defining the volume of interest and ascertained naturally

Table 2. Comparison between the two-dimensional and the present derivations of the image coordinates.

	Two-dimensional derivation	Present derivation	Equation
x_0	$X = \frac{-x_0 Z}{ML}$, $x_0 = \frac{x_{TR}+x_{TL}}{2}$	$X = \frac{-x_0 Z}{ML}$, $x_0 = \frac{x_{TR}+x_{TL}+x_B}{3}$	(9b)
y_0	$Y = \frac{-x_0 Z}{ML}$, $y_0 = \frac{y_{TR}+y_{TL}}{2}$	$Y = \frac{-y_0 Z}{ML}$, $y_0 = \frac{y_{TR}+y_{TL}+y_B}{3}$	(9d)
x_B	Not provided	$-\frac{M}{Z}[XL + \gamma(L-Z)] + \frac{2-\sqrt{3}}{2\sqrt{3}}h$	(7a)
x_{TR}	$-ML\frac{X}{Z}$	$-ML\frac{X}{Z}\left[1 - \frac{\gamma(L-Z)}{2XL}\right] + \frac{2-\sqrt{3}}{2\sqrt{3}}h$	(7b)
x_{TL}	$-ML\frac{X}{Z}$	$-ML\frac{X}{Z}\left[1 - \frac{\gamma(L-Z)}{2XL}\right] + \frac{2-\sqrt{3}}{2\sqrt{3}}h$	(7b)
y_B	Not provided	$y_B = -\frac{Yl}{Z}$	(7c)
y_{TR}	$\frac{M}{2Z}[-d(L-Z) - 2LY]$	$\frac{M}{2Z}[-d(L-Z) - 2LY]$	(7d)
y_{TL}	$\frac{M}{2Z}[d(L-Z) - 2LY]$	$\frac{M}{2Z}[d(L-Z) - 2LY]$	(7e)

Table 3. Comparison of the two-dimensional and the present derivations of the uncertainties of the system.

	Two-dimensional derivation	Present derivation	Equation
$\delta(dX)$	$K\lvert Z\rvert d\Delta x\sqrt{1 + \frac{2X^2}{d^2}}$	$\frac{\Delta x}{\sqrt{3}}K\lvert Z\rvert d\sqrt{1 + \frac{3X^2}{d^2}} = \Delta x K\lvert Z\rvert\gamma\sqrt{1 + \frac{X^2}{\gamma^2}}$	(19a)
$\delta(dY)$	$K\lvert Z\rvert d\frac{\Delta x}{\sqrt{2}}\sqrt{1 + \frac{4Y^2}{d^2}}$	$\frac{\Delta x}{\sqrt{3}}K\lvert Z\rvert d\sqrt{1 + \frac{3Y^2}{d^2}} = \Delta x K\lvert Z\rvert\gamma\sqrt{1 + \frac{Y^2}{\gamma^2}}$	(19b)
$\delta(dZ)$	$\sqrt{2}KZ^2\Delta x$	$KZ^2\Delta x$	(19c)
$\delta(db)$	$\sqrt{2}\Delta x$	Δx	(20)
$\frac{\delta(dZ)}{\delta(dY)}$	$\frac{2\lvert Z\rvert}{d\sqrt{1 + \left(\frac{2Y}{d}\right)^2}}$	$\frac{\sqrt{3}(\lvert Z\rvert/d)}{\sqrt{1 + \frac{3Y^2}{d^2}}} = \frac{(\lvert Z\rvert/\gamma)}{\sqrt{1 + \frac{Y^2}{\gamma^2}}}$	(21a)

from the geometry of the system. This has the advantage of reducing the number of input variables and intermediate variables required to define the geometric parameters d and Z_{min}, hence allowing for an easier camera design optimization process.

5.2. The effects of the asymmetrical lens locations in the X–Z plane on the image coordinates

Another benefit the full three-dimensional derivation has provided is the explicit derivation and expression of x_0 and y_0, which are needed to define the X and Y spatial coordinates. In PGDM and PG, the optical arrangement about the optical axis is symmetrical, corresponding to the Y–Z plane view shown in figure 12. Since their derivation is based on two pinholes, the third pinhole, (x_B, y_B), is not shown, and as a result, the expressions for x_0 and y_0 became a function of only two-particle image coordinates, (x_{TR}, y_{TR}) and (x_{TL}, y_{TL}), as shown in table 2. While PG have implicitly suggested the proper form of x_0 and y_0 after performing a two-dimensional derivation, the present three-dimensional derivation explicitly derives the proper expressions shown in equations (9b) and (9d). In addition, a comparison of the other two image coordinate pairs (x_{TR}, y_{TR}) and (x_{TL}, y_{TL}) between the two derivations is shown in table 2. While the y-components are identical between the two derivations, there is a stark contrast for the x-components: a reflection of the asymmetry in the X–Z plane (see figure 11) that was not considered in the two-dimensional derivation. In the present derivation, the x-components of the image coordinates were derived using the projection of the geometry onto the X–Z plane for guidance. Analogously, the y-components of the image coordinates were derived with the Y–Z projection of the system as a guide. As a result, the y-components naturally have identical expressions in both derivations. For the x-components, however, the present derivation includes the expression given in the two-dimensional derivation, as well as two additional terms. These two new terms are directly attributed to the asymmetry in the X–Z plane and the shifting term, respectively.

5.3. Uncertainty analysis

The derived uncertainties on displacements (dX, dY, dZ) are repeated in table 3 and compared with the results of PG. The distinction between the two-dimensional and full three-dimensional derivations of the uncertainties in the coordinates is not in the trends but in the detail. Specifically, all uncertainties are distinct and for fixed depth locations, $\delta(dX)$ and $\delta(dY)$ are minimized on the optical axis (equations (19a) and (19b)) while the uncertainties in dZ vary quadratically with Z and are independent of the X and Y coordinates. Because of the two-dimensional derivation of PG, the expressions for $\delta(dX)$ and $\delta(dY)$ are different in form, while the three-dimensional derivations show that these expressions are identical in form. In the present derivation, $\delta(dZ)$ is seen to be of the same form as the two-dimensional derivation, though smaller by a constant factor of $\sqrt{2}$. Hence, the two-dimensional derivations over-predicted the geometric uncertainties by 41%.

The ratio of the out-of-plane to the in-plane uncertainties, $\frac{\delta(dZ)}{\delta(dY)}$, as discussed earlier, follows the same trends as the plots published in PG. However, the present results show that this ratio is reduced by 13% for all points located on-axis. For points farther away from the axis, the uncertainties are reduced further from those reported in PG, such that at the maximum off-axis location, $\frac{Y}{d} = 1$, the uncertainties reach a maximum reduction of 39%.

One of the goals of describing the defocusing digital particle image velocimetry system three dimensionally is to understand how to design a system that would minimize the uncertainties. If all parameters can be characterized geometrically, then this optimization process can be carried out in a more systematic manner if limits of their values can be determined *a priori*. However, if more parameters are given as inputs, as in the case of the two-dimensional derivation, the process of optimization becomes more tedious, unless there are circumstances where input parameters are specified due to other constraints. One way to reduce the uncertainties, is to reduce the uncertainty ratio, $\frac{\delta(dZ)}{\delta(dY)}$, shown in table 3. Note that by increasing the distance of the lens from the optical axis, γ, this uncertainty ratio will decrease. This trend, however, is not evident in the in-plane uncertainties, $\delta(dX)$ and $\delta(dY)$, as increasing γ will increase these uncertainties; and in the out-of-plane uncertainty, $\delta(dZ)$, as increasing γ will decrease this uncertainty, as can be seen in table 3. Therefore, a compromise must be achieved based on the design requirements of the system that dictate γ and hence d (see equation (6)), and the error ratio. A second way to reduce the uncertainties is to decrease the range of Z by decreasing the distance between the volume of interest and the lens plane. Finally, the uncertainties can be reduced by considering the separation gradient, $\frac{\partial b}{\partial Z}$. Intuitively, it would seem that if the system sensitivity is increased, the geometric uncertainties would decrease. This is in fact verified by expressing the geometric uncertainties $\delta(dX), \delta(dY)$ and $\delta(dZ)$ in terms of the separation gradient $\frac{\partial b}{\partial Z}$,

$$\delta(dX) = -\frac{\Delta x}{\frac{\partial b}{\partial Z}\left(\frac{|Z|}{\gamma}\right)}\sqrt{1+\frac{X^2}{\gamma^2}} \quad (22a)$$

$$\delta(dY) = -\frac{\Delta x}{\frac{\partial b}{\partial Z}\left(\frac{|Z|}{\gamma}\right)}\sqrt{1+\frac{Y^2}{\gamma^2}} \quad (22b)$$

$$\delta(dZ) = \frac{1}{\left(\frac{\partial b}{\partial Z}\right)}\Delta x, \quad (22c)$$

where the separation gradient appears in the denominator. From these expressions, it can be seen that minimizing the separation gradient (maximizing its absolute value) will yield smaller uncertainties.

6. Conclusion

In summary, the present derivation affords the complete characterization of the system using equations with fewer inputs than is required by those presented by PGDM and subsequently PG and assists in the optimization process of a three-dimensional DDPIV camera system. This was done by eliminating the idea of an indirect cubic representation of the volume of interest and replacing it with a more relevant triangular volume of interest. The lens separation distance can now be expressed through a geometric equation, and Z_{min} now is dependent only upon the location and dimensions of the triangular domain of interest. Furthermore, by incorporating a full three-dimensional analysis, the asymmetrical nature of the geometry in the X–Z plane showed that all the x-components of the image coordinates became functions of the radial distance

of the pinholes from the optical axis, γ, rather than the separation between pinholes, d. Similarly shown is that γ, and not d, is the proper non-dimensionalization parameter for the spatial coordinates in the expressions for the geometric uncertainties. These resulted in expressions that accurately describe the optics of this technique, as well as uncertainties that better reflect the performance of the defocusing DPIV system.

Beyond these improvements, one recommendation would be to incorporate the radius of curvature of the volume of interest (see figure 8). Although this may significantly add to the complexity of the equations, the derivation will allow the volume of interest to fully incorporate the full lateral extent of the observable domain. A second recommendation to improve the present derivation would be to include the effects of aberrations and their effects on particle identification, for cases where the F number is small and these effects are significant. These recommendations collectively will allow further improvements and advancements in our ability to completely characterize the geometry of three-dimensional DDPIV to assist in design and optimization processes.

References

Adrian R J 1986 Multi-point optical measurements of simultaneous vectors in unsteady flow: a review *Int. J. Heat Fluid Flow* **7** 127–45
Adrian R J 1991 Particle-imaging techniques for experimental fluid-mechanics *Ann. Rev. Fluid Mech.* **23** 261–304
Adrian R J and Yao C S 1983 Development of pulsed laser velocimetry for measurements of fluid flow *Proc. 8th Biennial Symp. on Turbulence (University of Missouri, Rolla, MO)*
Arroyo M P and Greated C A 1991 Stereoscopic particle image velocimetry *Meas. Sci. Technol.* **2** 1181–6
Barnheart D H, Adrian R J and Papen G C 1994 Phase-conjugate holographic system for high-resolution particle-image velocimetry *Appl. Opt.* **33** 7159–70
Cowen E A and Monismith S G 1997 A hybrid digital particle tracking velocimetry technique *Exp. Fluids* **22** 199–211
Gharib M, Modarress D, Dabiri D, Pereira F and Taugwalder F 1998 Development and application of a defocusing three dimensional DPIV technique for the mapping of two-phase bubbly flows *Proc. 9th Int. Symp. on Applications of Laser Techniques to Fluid Mechanics (Instituto Superior Technico, Lisbon, Portugal)*
Huang H T, Fiedler H E and Wang J J 1993a Limitation and improvement of PIV: I. Limitation of conventional techniques due to deformation of particle image patterns *Exp. Fluids* **15** 168–74
Huang H T, Fiedler H E and Wang J J 1993b Limitation and improvement of PIV: II. Particle image distortion, a novel technique *Exp. Fluids* **15** 263–73
Lawson N J and Wu J 1997 Three-dimensional particle image velocimetry: error analysis of stereoscopic techniques *Meas. Sci. Technol.* **8** 894–900
Meng H and Hussain F 1995 In-line recording and off-axis viewing (IROV) technique for holographic particle velocimetry *Appl. Opt.* **34** 1827–40
Murai S, Nakamura H and Suzaki Y 1980 Analytical orientation for non-metric camera in the application to terrestrial photogrametry *Int. Arch. Photogramm.* **23** 516–25

Nogueira J, Lecuona A, Ruiz-Rivas U and Rodriguez P A 2002 Analysis and alternatives in two-dimensional multigrid particle image velocimetry methods: application of a dedicated weighting function and symmetric direct correlation *Meas. Sci. Technol.* **13** 963–74

Pereira F and Gharib M 2002 Defocusing digital particle image velocimetry and the three-dimensional characterization of two-phase flows *Meas. Sci. Technol.* **13** 683–94

Pereira F, Gharib M, Dabiri D and Modarress D 2000 Defocusing digital particle image velocimetry. A 3-component 3-dimensional DPIV measurement technique: application to bubbly flows *Exp. Fluids* **29** S78–84

Ponchaut N F, Mouton C A and Hornung H G 2004 Development of three-dimensional particle tracking velocimetry for supersonic flow *AIAA Paper, 42nd AIAA Aerospace Sciences Meeting and Exhibit* pp 7822–31

Raffel M, Willert C and Kompenhans J 1998 *Particle Image Velocimetry: A Practical Guide* (Berlin: Springer)

Virant M and Dracos T 1997 3D PTV and its application on Lagrangian motion *Meas. Sci. Technol.* **8** 1539–52

Webster D R, Roberts P J W and Ra'ad L 2001 Simultaneous DPTV/PLIF measurements of a turbulent jet *Exp. Fluids* **30** 65–72

Westerweel J 1993 *Digital Image Velocimetry: Theory and Application* (Delft: Delft University Press)

Westerweel J, Dabiri D and Gharib M 1997 The effect of a discrete window offset on the accuracy of cross-correlation analysis of digital PIV recordings *Exp. Fluids* **23** 20–8

Willert C 1997 Stereoscopic digital particle image velocimetry for application in wind tunnel flows *Meas. Sci. Technol.* **8** 1465–79

Willert C and Gharib M 1991 Digital particle image velocimetry *Exp. Fluids* **10** 181–3

Willert C and Gharib M 1992 Three-dimensional particle imaging with a single camera *Exp. Fluids* **12** 353–8

Zhang J, Tao B and Katz J 1997 Turbulent flow measurement in a square duct with hybrid holographic PIV *Exp. Fluids* **23** 373–81

Zimin V, Meng H and Hussain F 1993 Innovative holographic particle velocimeter: a multibeam technique *Opt. Lett.* **18** 1101–3